A Generalised Mathematical Representation of the Shape of the Wheatley Heart Valve and the Associated Static Stress Fields upon Opening and Closing

H. L. Oliveira*[a], S. McKee[b], G. C. Buscaglia[a], J. A. Cuminato[a], I. W. Stewart[b], D. J. Wheatley[c]

[a]*Instituto de Ciências Matemáticas e de Computação - ICMC, Universidade de São Paulo - Campus de São Carlos, Caixa Postal 668, 13560-970 São Carlos-SP, Brasil*
[b]*Department of Mathematics and Statistics, University of Strathclyde, Glasgow, UK*
[c]*School of Science and Engineering, University of Dundee, Dundee, UK*

Abstract

This note extends previous work of the authors modelling the Wheatley valve by using six intersecting and contiguous ellipses to obtain a generalised mathematical representation of the Wheatley valve: this provides a number of free parameters which could be employed to obtain an optimal design. Since optimality is multi-objective with many of the objectives conflicting we focus on the stresses imposed on the valve by a constant force field. Three distinctly different designs are chosen and an analysis of the stresses is undertaken, conclusions are drawn and results are discussed.

Keywords: Wheatley heart valve, mathematical description, non-linear mechanical model, finite element method

1. Introduction

Computational modelling plays a crucial role in the search for improved designs in various fields of science and engineering: it allows the designer to gain insight by varying the input parameters, and so optimize his or her design. With advent of high-speed computers, numerical modelling has now been recognised as the "third pillar of science" alongside the other two: theory and experiment (Riedel et al. (2008)).

Email address: hugo.oliveira@icmc.usp.br (H. L. Oliveira*)

This is particularly true in the case of artificial heart valve applications (Kaiser et al. (2021)). Indeed, mathematical models can be an important tool for the better understanding of complex cardiovascular systems, especially when other techniques are only accessible indirectly, or in a limited way (Jatene et al. (1999); Ghanbari et al. (2022)). For instance, topology optimization, initially applied to structural mechanics (Bendsøe (1989)), has been suggested as a means of capturing the complex shape of *in vitro* mitral valve (Khalighi et al. (2019)). In another study, Jenkins and Maute (2016) suggested that leaflet geometry could be determined by a combination of boundary capture techniques (level-set based) and topology or shape optimization. For patient-specific treatments, Balu et al. (2019) suggested using Deep Learning to build mechanical models that are functionally equivalent to real valves using medical imaging.

Phase contrast magnetic resonance imaging has demonstrated unfavourably altered flow patterns in the ascending aorta after aortic valve replacement with both mechanical and bioprosthetic valves as compared with normal aortic flow patterns Jarral et al. (2020). To address this problem, the sixth author – which has a long-standing research experience in the field of heart valve replacement surgery (Chaudhry et al. (2000); Wheatley et al. (2000)) and holds a number of patents in this area (Wheatley (2014, 2016a,b)) – developed a novel design which has become known as the Wheatley heart valve (WHV). The Wheatley design is intended to function in conjunction with a spiral flow pattern to aid valve opening while retaining spiral flow throughout the cardiac cycle in the expectation of reducing thrombogenicity.

The experimental WHVs have not consistently demonstrated satisfactory durability or low thrombogenicity. In order to show that this novel design is likely to meet these essential clinical expectations it will be important to be able to predict the stress on the valve's leaflets and the flow patterns within the ascending aorta both with a natural valve and with the novel aortic valve in place. Some numerical techniques have been applied quite successfully for this purpose such as Immersed Boundary approaches (e.g. Peskin (1972); Wang and Zhang (2013); Sun et al. (2014)) and Arbitrary Lagrangian-Eulerian approaches (eg. Spühler et al. (2018)). We refer the reader to Abbas et al. (2022) for an overview of the aortic valve simulation process. Despite this, models that address WHVs behaviour are not yet available.

The contribution of the present study is twofold. The first is to present a new analytical expression describing the geometry of leaflets for WHVs.

This new expression employs contiguous and intersecting ellipses, which in turn encompasses and expands upon the equations presented by the authors previously (McKee et al. (2021)). The second consists in proposing a mechanical model capable of simulating the opening and closing movements of the WHV. The proposed expression is used to generate three geometries that are used as input to the mechanical model. Additional aspects of the model are: use of shell elements to represent the leaflets, linearity of the material constitutive response, evaluation of the equilibrium always in the displaced position, inter-leaflets non-linear contact to ensure appropriate opening and closing motions.

2. Analytical description of the leaflet surfaces

2.1. The artificial aortic valve

The Wheatley valve is displayed in Figure 1. As previously mentioned McKee et al. (2021), the authors have developed a mathematical representation of the shape of this valve using six intersecting and contiguous circles to model the contour lines/level set. These were then extended in the vertical direction (z-direction) and the surface of the resulting three dimensional object was seen to be a mathematical replica of the Wheatley valve (see Figure 2).

Figure 1: The Wheatley Valve. The height is 13 mm and the outer diameter is 25 mm; the inner orifice diameter is 23mm. A typical leaflet thickness is 150 microns.
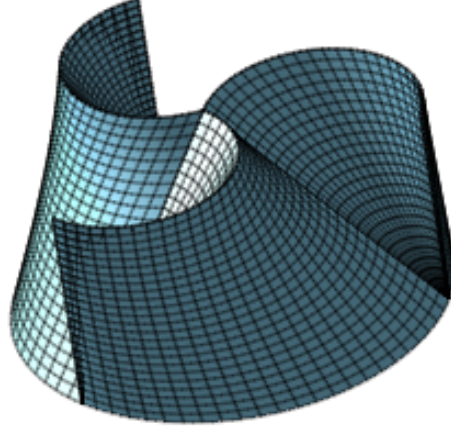
3

Figure 2: Mathematical representation of the Wheatley valve (McKee et al. (2021))

2.2. Two contiguous ellipses

In order to construct a generalisation of the Wheatley valve we shall consider the six ellipses embedded within the unit circle as shown in Figure 3.

In this section we shall focus on the two contiguous ellipses BPP' and BP''. It will be readily observed that the two ellipses $B'P'P''$ and $B'P$ are identical to the original two, once they have been rotated clockwise through $\frac{4}{3}\pi$. Similarly, ellipses $B''P''P$ and $B''P'$ are also identical with the original two after clockwise rotation through $\frac{2}{3}\pi$.

Referring to Figure 3 we note that the equation of the ellipse BPP' in x', y'-coordinates is

$$\frac{x'^2}{a^2} + \frac{y'^2}{b^2} = 1 \tag{1}$$

where a and b denote, respectively, the major axis and minor axis of the ellipse. Here C denotes the centre of the ellipse BPP', while S denotes the centre of the ellipse BP''. Let $|OA| = \alpha$ and let $|OP''| = \beta$. From symmetry, $|OP| = |OP'| = \beta$. Then, since $|OB| = 1$, $|CB| = |CA| = \frac{1}{2}(1 + \alpha)$ and $|SP''| = |SB| = \frac{1}{2}(1 - \beta)$ and $|OS| = \frac{1}{2}(1 + \beta)$.

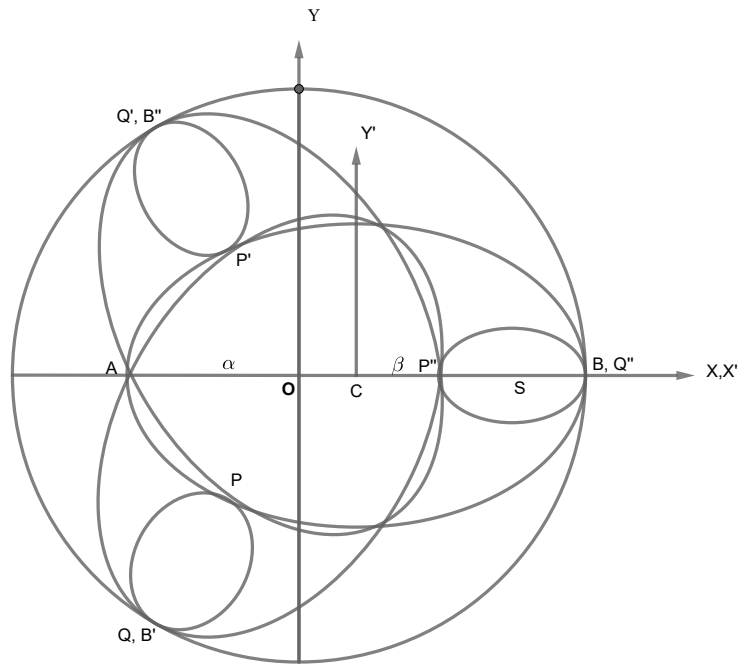Since $a = |CB| = \frac{1}{2}(1 + \alpha)$, equation (1) becomes

4

Figure 3: Six intersecting and contiguous ellipses embedded in the unit circle

$$\frac{x'^2}{\left[\frac{1}{2}(1+\alpha)\right]^2} + \frac{y'^2}{b^2} = 1. \tag{2}$$

Now, in the (x, y)-coordinate system, the ellipse (2) becomes

$$\frac{\left[x - \frac{1}{2}(1-\alpha)\right]^2}{\left[\frac{1}{2}(1+\alpha)\right]^2} + \frac{y^2}{b^2} = 1, \tag{3}$$

since $|OC| = |CA| - |OA| = \dfrac{1}{2}(1-\alpha)$.

This ellipse must pass through the points $B(1,0)$, $A(-\alpha,0)$, $P\left(-\dfrac{1}{2}\beta, -\dfrac{\sqrt{3}}{2}\beta\right)$ and $P'\left(-\dfrac{1}{2}\beta, \dfrac{\sqrt{3}}{2}\beta\right)$. The first two points A and B are clearly satisfied; the

5

second two P and P' both lead to the same requirement:

$$\frac{\left[-\frac{1}{2}\beta - \frac{1}{2}(1-\alpha)\right]^2}{\left[\frac{1}{2}(1+\alpha)\right]^2} + \frac{\frac{3}{4}\beta^2}{b^2} = 1 \quad \Longrightarrow \quad b^2 = \frac{3\beta^2(1+\alpha)^2}{4(2\alpha - \beta)(2+\beta)}$$

Since b must be positive,

$$b = \frac{\sqrt{3}\beta(1+\alpha)}{2\sqrt{(2\alpha - \beta)(2+\beta)}}. \tag{4}$$

Thus the ellipse BPP' is given by

$$\frac{\left[x - \frac{1}{2}(1-\alpha)\right]^2}{\left[\frac{1}{2}(1+\alpha)\right]^2} + \frac{y^2}{\gamma^2 \left[\frac{1}{2}(1+\alpha)\right]^2} = 1 \tag{5}$$

where

$$\gamma = \frac{\sqrt{3}\beta}{\sqrt{(2\alpha - \beta)(2+\beta)}}. \tag{6}$$

In the following we shall use γ as a measure of the 'degree of ellipticity'.

Let us now consider Figure 4.

In the x'', y''-coordinate system, the ellipse BP'' can be written as

$$\frac{x''^2}{\tilde{a}^2} + \frac{y''^2}{\tilde{b}^2} = 1, \tag{7}$$

where, again, the major and minor axes are denoted by $\tilde{a}$ and $\tilde{b}$, respectively. In x, y-coordinates equation (7) becomes

$$\frac{\left[x - \frac{1}{2}(1+\beta)\right]^2}{\tilde{a}^2} + \frac{y^2}{\tilde{b}^2} = 1. \tag{8}$$

We note that $\tilde{a} = |SB| = \frac{1}{2}(1-\beta)$ and so equation (8) becomes

$$\frac{\left[x - \frac{1}{2}(1+\beta)\right]^2}{\left[\frac{1}{2}(1-\beta)\right]^2} + \frac{y^2}{\tilde{b}^2} = 1. \tag{9}$$

Equation (9) must pass through $B(1,0)$ and $P''(\beta, 0)$. Both are automatically satisfied. Two further conditions are required:
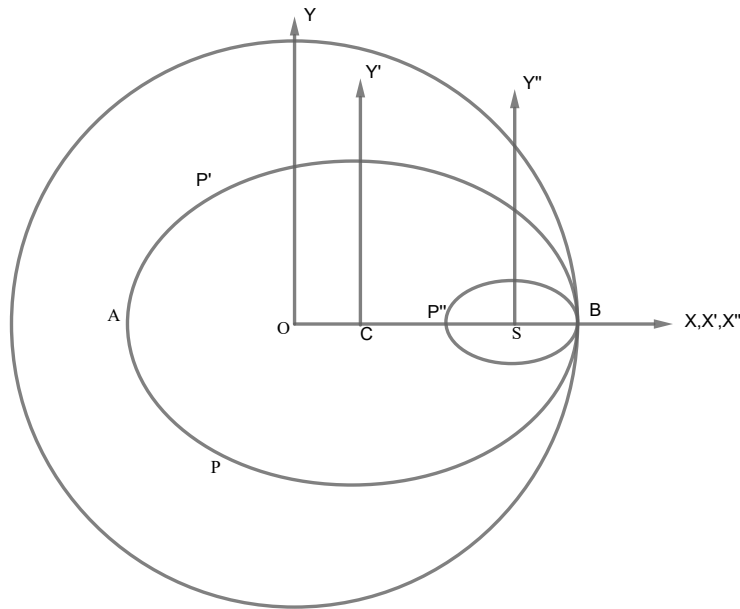
6

Figure 4: Two contiguous ellipses within the unit circle

(A) As α and β tend to 1 (at the same rate) the ellipse BPP' must tend to the unit circle.

(B) The ratio of the major to minor axes of the ellipse BPP' must be the same as the ratio of the major to minor axes of the ellipse BP'' (i.e. $\dfrac{a}{b} = \dfrac{\tilde{a}}{\tilde{b}}$).

Condition (B) is required because as α and $\beta \to 0$ the ellipse BPP' coalesces into the ellipse BP''.

It is readily seen that equation (9) satisfies condition (A) provided α and $\beta \to 1$ at the same rate.

Condition (B), however, leads to

$$\tilde{b} = \frac{\sqrt{3}\beta(1-\beta)}{2\sqrt{(2\alpha - \beta)(2+\beta)}}, \tag{10}$$

since $\tilde{b} > 0$.

Thus the subsidiary ellipse BP'' is

7

$$\frac{\left[x - \frac{1}{2}(1 + \beta)\right]^2}{\left[\frac{1}{2}(1 - \beta)\right]^2} + \frac{y^2}{\gamma^2 \left[\frac{1}{2}(1 - \beta)\right]^2} = 1, \tag{11}$$

where γ is given by equation (6).

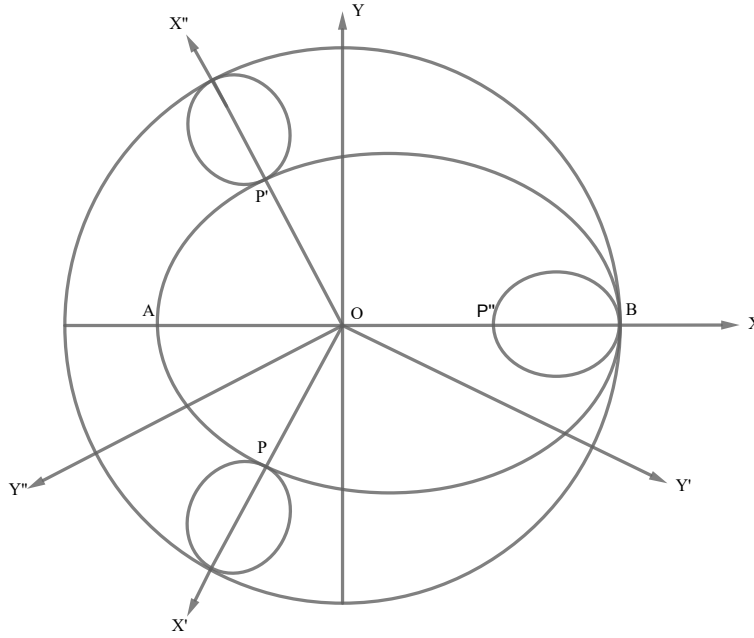### 2.3. Two further sets of ellipses

Figure 5: Ellipses and rotation of axes

Consider Figure 5. As has already been stated, the two sets of ellipses $B'P'P''$, $B''P''P$ and PQ, $P'Q'$ (see Figure 3) are equivalent to the ellipses BPP' and $P''Q''$ after suitable rotations.

2.3.1. Ellipses $\boldsymbol{B'P'P''}$ and $\boldsymbol{PQ}$

The ellipses $B'P'P''$ and PQ in the x', y'-coordinate system are

$$\frac{\left[x' - \frac{1}{2}(1 - \alpha)\right]^2}{\left[\frac{1}{2}(1 + \alpha)\right]^2} + \frac{y'^2}{\gamma^2 \left[\frac{1}{2}(1 + \alpha)\right]^2} = 1 \tag{12}$$

8

and

$$\frac{\left[x' - \frac{1}{2}(1 + \beta)\right]^2}{\left[\frac{1}{2}(1 - \beta)\right]^2} + \frac{y'^2}{\gamma^2 \left[\frac{1}{2}(1 - \beta)\right]^2} = 1. \tag{13}$$

Clockwise axes rotation through $\frac{4}{3}\pi$ is given by

$$\begin{aligned}
x' &= x \cos \frac{4}{3}\pi + y \sin \frac{4}{3}\pi &= -\frac{1}{2}x - \frac{\sqrt{3}}{2}y, \\
y' &= -x \sin \frac{4}{3}\pi + y \cos \frac{4}{3}\pi &= \frac{\sqrt{3}}{2}x - \frac{1}{2}y.
\end{aligned}$$

Thus, the equations of the ellipses (12) and (13) become

$$\frac{\left[-\frac{1}{2}x - \frac{\sqrt{3}}{2}y - \frac{1}{2}(1 - \alpha)\right]^2}{\left[\frac{1}{2}(1 + \alpha)\right]^2} + \frac{\left[\frac{\sqrt{3}}{2}x - \frac{1}{2}y\right]^2}{\gamma^2 \left[\frac{1}{2}(1 + \alpha)\right]^2} = 1, \tag{14}$$

$$\frac{\left[-\frac{1}{2}x - \frac{\sqrt{3}}{2}y - \frac{1}{2}(1 + \beta)\right]^2}{\left[\frac{1}{2}(1 - \beta)\right]^2} + \frac{\left[\frac{\sqrt{3}}{2}x - \frac{1}{2}y\right]^2}{\gamma^2 \left[\frac{1}{2}(1 - \beta)\right]^2} = 1, \tag{15}$$

or

$$\frac{\left[x + \sqrt{3}y + (1 - \alpha)\right]^2}{(1 + \alpha)^2} + \frac{\left[\sqrt{3}x - y\right]^2}{\gamma^2(1 + \alpha)^2} = 1 \tag{16}$$

and

$$\frac{\left[x + \sqrt{3}y + (1 + \beta)\right]^2}{(1 - \beta)^2} + \frac{\left[\sqrt{3}x - y\right]^2}{\gamma^2(1 - \beta)^2} = 1. \tag{17}$$

2.3.2. Ellipses $B''P''P$ and $P'Q'$

In the x'', y''-coordinate system the ellipses B"P"P and P'Q' may be written, respectively, as

$$\frac{\left[x'' - \frac{1}{2}(1 - \alpha)\right]^2}{\left[\frac{1}{2}(1 + \alpha)\right]^2} + \frac{y''^2}{\gamma^2 \left[\frac{1}{2}(1 + \alpha)\right]^2} = 1 \tag{18}$$

9

and

$$\frac{\left[x'' - \frac{1}{2}(1+\beta)\right]^2}{\left[\frac{1}{2}(1-\beta)\right]^2} + \frac{y''^2}{\gamma^2 \left[\frac{1}{2}(1-\beta)\right]^2} = 1. \tag{19}$$

Axes rotation clockwise through $\frac{2}{3}\pi$ is given by

$$\begin{array}{rclcl} x'' & = & x\cos\frac{2}{3}\pi + y\sin\frac{2}{3}\pi & = & -\frac{1}{2}x + \frac{\sqrt{3}}{2}y, \\ y'' & = & -x\sin\frac{2}{3}\pi + y\cos\frac{2}{3}\pi & = & -\frac{\sqrt{3}}{2}x - \frac{1}{2}y. \end{array}$$

Thus equations (18) and (19) become

$$\frac{\left[-\frac{1}{2}x + \frac{\sqrt{3}}{2}y - \frac{1}{2}(1-\alpha)\right]^2}{\left[\frac{1}{2}(1+\alpha)\right]^2} + \frac{\left[-\frac{\sqrt{3}}{2}x - \frac{1}{2}y\right]^2}{\gamma^2 \left[\frac{1}{2}(1+\alpha)\right]^2} = 1 \tag{20}$$

and

$$\frac{\left[-\frac{1}{2}x + \frac{\sqrt{3}}{2}y - \frac{1}{2}(1+\beta)\right]^2}{\left[\frac{1}{2}(1-\beta)\right]^2} + \frac{\left[-\frac{\sqrt{3}}{2}x - \frac{1}{2}y\right]^2}{\gamma^2 \left[\frac{1}{2}(1-\beta)\right]^2} = 1, \tag{21}$$

or

$$\frac{[-x + \sqrt{3}y - (1-\alpha)]^2}{(1+\alpha)} + \frac{[\sqrt{3}x + y]^2}{\gamma^2(1-\beta)^2} = 1 \tag{22}$$

and

$$\frac{[-x + \sqrt{3}y - (1+\beta)]^2}{(1-\beta)^2} + \frac{[\sqrt{3}x + y]^2}{\gamma^2(1-\beta)^2} = 1. \tag{23}$$

2.4. Parametrisation

In order to construct the surface of the generalised Wheatley valve we require the following sequence of arcs: BP (clockwise), PQ (anticlockwise), $B'P'$ (clockwise), $P'Q'$ (anticlockwise), $B''P''$ (clockwise), $P''Q''$ (anticlockwise). Thus we need to consider the ellipses (or the appropriate arcs of these) in the following order: (5), (17), (16), (23), (22) and (11).

For equation (5) we write

$$\frac{x - \frac{1}{2}(1-\alpha)}{\frac{1}{2}(1+\alpha)} = \cos t, \quad \frac{y}{\frac{1}{2}\gamma(1+\alpha)} = \sin t$$

10

giving

$$x = \frac{1}{2}[1 - \alpha + (1 + \alpha)\cos t] \tag{24a}$$

$$y = \frac{1}{2}\gamma(1 + \alpha)\sin t \tag{24b}$$

For equation (17) write

$$x + \sqrt{3}y = -(1 + \beta) + (1 - \beta)\cos t,$$
$$\sqrt{3}x - y = \gamma(1 - \beta)\sin t.$$

Solving for x and y gives

$$x = \frac{1}{4}\left[-(1 + \beta) + (1 - \beta)\cos t + \sqrt{3}\gamma(1 - \beta)\sin t\right] \tag{25a}$$

$$y = \frac{1}{4}\left[\sqrt{3}(-(1 + \beta) + (1 - \beta)\cos t) - \gamma(1 - \beta)\sin t\right] \tag{25b}$$

To obtain the correct arc for $B'P'$ we must select (14) as opposed to (16). Thus we write

$$-x - \sqrt{3}y = (1 - \alpha) + (1 + \alpha)\cos t,$$
$$\sqrt{3}x - y = \gamma(1 + \alpha)\sin t.$$

Solving for x and y gives

$$x = \frac{1}{4}\left[-(1 - \alpha) - (1 + \alpha)\cos t + \sqrt{3}\gamma(1 + \alpha)\sin t\right] \tag{26a}$$

$$y = -\frac{1}{4}\left[\sqrt{3}\left((1 - \alpha) + (1 + \alpha)\cos t\right) + \gamma(1 + \alpha)\sin t\right] \tag{26b}$$

For equation (23) we write

$$-x + \sqrt{3}y = (1 + \beta) + (1 - \beta)\cos t,$$
$$\sqrt{3}x + y = \gamma(1 - \beta)\sin t,$$

resulting in

11

$$x = \frac{1}{4}\left[-(1+\beta) - (1-\beta)\cos t + \sqrt{3}\gamma(1-\beta)\sin t\right] \tag{27a}$$

$$y = \frac{1}{4}\left[\sqrt{3}(1+\beta + (1-\beta)\cos t) + \gamma(1-\beta)\sin t\right] \tag{27b}$$

Once again to obtain the correct arc for $B''P''$ we must select (20) as opposed to (22). Thus we write

$$-x + \sqrt{3}y = (1-\alpha) + (1+\alpha)\cos t,$$
$$-\sqrt{3}x - y = \gamma(1+\alpha)\sin t,$$

leading to

$$x = -\frac{1}{4}\left[1 - \alpha + (1+\alpha)\cos t + \sqrt{3}\gamma(1+\alpha)\sin t\right] \tag{28a}$$

$$y = \frac{1}{4}\left[\sqrt{3}(1 - \alpha + (1+\alpha)\cos t) - \gamma(1+\alpha)\sin t\right] \tag{28b}$$

Finally, for arc $P''Q''$ we have (from equation (11))

$$x = \frac{1}{2}(1+\beta) + \frac{1}{2}(1-\beta)\cos t \tag{29a}$$

$$y = \frac{\gamma}{2}(1-\beta)\sin t \tag{29b}$$

2.5. Constructing the three dimensional surface

2.5.1. Degree of ellipticity

It is clear that the equations (5), (16) and (22) for the ellipses BPP', $B'P'P''$ and $B''P''P$ reduce to circles when the parameter γ is unity, i.e. when
$$\frac{\sqrt{3}\beta}{\sqrt{(2\alpha - \beta)(2+\beta)}} = 1.$$
This will occur when

$$\alpha = \frac{\beta(2\beta + 1)}{(2+\beta)} \tag{30}$$

12

or, equivalently, when

$$\beta^2 + \frac{1}{2}(1 - \alpha)\beta - \alpha = 0$$

or

$$2\beta = -\frac{1}{2}(1 - \alpha) + \sqrt{\frac{1}{4}(1 - \alpha)^2 + 4\alpha},$$

the negative value having been discarded since $\beta \geq 0$. Since $\alpha, \beta \in [0, 1]$ and $\alpha, \beta \to 1$ and $\alpha, \beta \to 0$ at the same rate a reasonable relationship between α and β might be

$$\alpha = \nu \left(\frac{\beta(2\beta + 1)}{(2 + \beta)} \right)^n \tag{31}$$

where $\nu > 0$ and n are free parameters.

2.5.2. The third dimension

The third dimension is, of course, the vertical z-direction. Having eliminated α through equation (31) we could choose $z = \beta$, and let β run from 0 to 1. This would certainly allow us to construct the closed valve. However, it would be useful if a valve could be simulated at different stages of opening. This could be achieved by selecting

$$z = \frac{\beta - \kappa}{1 - \kappa},$$

where κ is a measure of how open the value is; in this case β would run from κ to 1. There is, however, no need for z to depend linearly on β, so instead we could choose

$$z = \left(\frac{\beta - \kappa}{1 - \kappa} \right)^m, \tag{32}$$

with again β running from κ to 1. For example, if $m = 2$ we would obtain a quadratic or parabolic profile as opposed to a linear increase in z. (Furthermore, we can allow each leaflet to open at a different rate by selecting κ_1, κ_2 and κ_3 (corresponding to each leaflet) in (32); indeed, there is the further possibility of choosing m_1, m_2 and m_3 in place of just m in (32).)

13

With (31) and (32) we have introduced three parameters ν, n and m, all of which will have an influence on the final shape of the valve, and may possibly allow a degree of design optimisation.

Nevertheless, we must still trace the correct arcs BP, PQ, $B'P'$, $P'Q'$, $B''P''$, $P''Q''$. Obtaining the desired arcs is not trivial and does require determining the correct starting and end points for each arc. The next section will provide these.

2.6. Starting and end points for the six arcs

Let t_B and t_P denote the start and end point for the arc BP and t_P (generally different from the value t_P for the arc BP) and t_Q denote the start and end point for the arc PQ with similar notation for the remaining arcs. We require the following:

Arc BP: $\quad t_B = 2\pi, t_P = \pi + \cos^{-1}\left[\frac{1-\alpha+\beta}{1+\alpha}\right]$

Arc PQ: $\quad t_P = 2\pi, \ t_Q = \pi$

Arc $B'P'$: $\quad t_{B'} = 2\pi, \ t_{P'} = \pi + \cos^{-1}\left[\frac{1-\alpha+\beta}{1+\alpha}\right]$

Arc $P'Q'$: $\quad t_{P'} = 0, \ t_{Q'} = \pi$

Arc $B''P''$: $\quad t_{B''} = 2\pi, \ t_{P''} = \pi + \cos^{-1}\left[\frac{1-\alpha+\beta}{1+\alpha}\right]$

Arc $P''Q''$: $\quad t_{P''} = -\pi, \ t_{Q''} = 0$

where, in this case, α is to be replaced with (31), that is,

$$\alpha = \nu \left(\frac{\beta(2\beta+1)}{2+\beta}\right)^n.$$

2.7. Possible generalised designs of the Wheatley valve

There are four parameters characterising the generalised mathematical representation of the valve, namely, ν, n, m and κ. Both ν and n contribute to the degree of ellipticity, or, equivalently, the degree to which the valve deviates from the previous circular design (e.g.McKee et al. (2021)). The parameter m is a measure of the deviation from linearity when constructing the side walls. For example, $m = 2$ produces a quadratic or parabolic shape. Finally, we note that κ is a measure of the degree of 'openness' of the valve. To illustrate the many possible generalisations of the original Wheatley valve,

14

Figure 6(a-c) shows a highly elliptic shape with linear vertical walls. Figure 7(a-c) displays a slightly elliptic shape with curved vertical walls. Finally, Figure 8(a-c) depicts a circular shape with strongly curved vertical walls (i.e. $m = 8$).
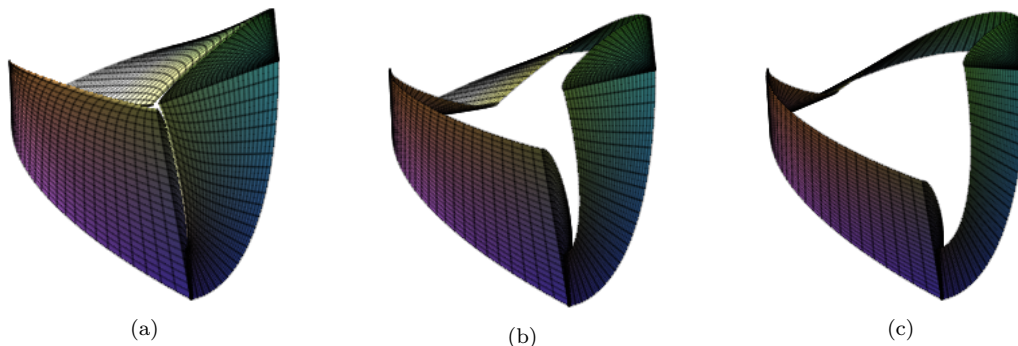

(a)
(b)
(c)

Figure 6: Valve with parameters: (a) $\nu = 5, m = n = 1, \kappa = 0$, (b) $\nu = 5, n = m = 1, \kappa = 0.25$, (c) $\nu = 5, m = n = 1, \kappa = 0.5$
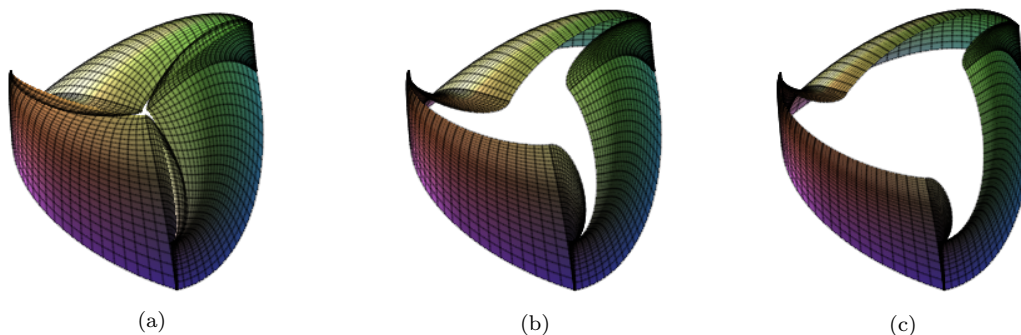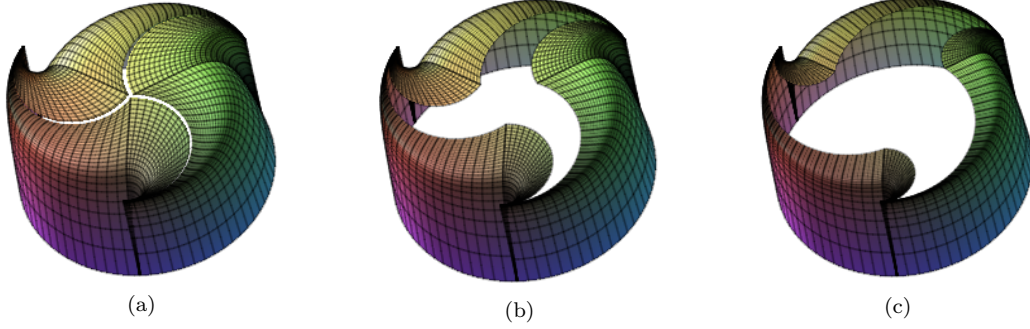

(a)
(b)
(c)

Figure 7: Valve with parameters: (a) $\nu = 2, n = 1, m = 4, \kappa = 0$, (b) $\nu = 2, n = 1, m = 4, \kappa = 0.25$, (c) $\nu = 2, n = 1, m = 4, \kappa = 0.5$

3. Mechanical model

3.1. Boundary Value Problem

Let $\Omega \subset \mathbb{R}^n$ (with $n = 1, 2, 3$) represent a portion of solid material that constitutes the valve, and $t \in [0, T]$ be the pseudo-time. The actions that surroundings exert on the valve occur through surface forces ($\bar{\mathbf{p}}$ applied on

15

Figure 8: Valve with parameters: (a) $\nu = 1, n = 1, m = 8, \kappa = 0$, (b) $\nu = 1, n = 1, m = 8, \kappa = 0.25$, (c) $\nu = 1, n = 1, m = 8, \kappa = 0.5$

$\partial\Omega_p$), displacements ($\bar{\mathbf{u}}$ applied on $\partial\Omega_u$) and body forces ($\mathbf{b}$ applied on Ω). The boundary is complementary ($\partial\Omega_p \cup \partial\Omega_u = \partial\Omega$) and $\mathbf{n}$ denotes the outward normal vector. A point in the initial configuration ($t = 0$) is denoted by $\mathbf{X}$ and at the current configuration by $\mathbf{x}$, such as $\mathbf{x} = \mathbf{X} + \mathbf{u}$. Solving the boundary value problem (BVP) consists in finding the displacement field $\mathbf{u} = \mathbf{u}(\mathbf{X}, \mathbf{t})$ such that:

$$\nabla \cdot \boldsymbol{\sigma}(\mathbf{u}) + \mathbf{b} = 0 \qquad\qquad \mathbf{x} \in \boldsymbol{\Omega} \qquad (33)$$

$$\boldsymbol{\sigma}(\mathbf{u}) = \mathcal{A}(\boldsymbol{\epsilon}(\mathbf{u})) \qquad\qquad \mathbf{x} \in \boldsymbol{\Omega} \qquad (34)$$

$$\mathbf{u} = \bar{\mathbf{u}} \qquad\qquad \mathbf{x} \in \partial\boldsymbol{\Omega_u} \qquad (35)$$

$$\boldsymbol{\sigma}(\mathbf{u})\mathbf{n} = \mathbf{p} = \bar{\mathbf{p}} \qquad\qquad \mathbf{x} \in \partial\boldsymbol{\Omega_p} \qquad (36)$$

where "$\nabla\cdot$" denotes the divergence operator, $\boldsymbol{\sigma}(\mathbf{u})$ stands for the Cauchy stress tensor, $\boldsymbol{\epsilon}(\mathbf{u})$ is the strain tensor and $\mathcal{A}$ is the constitutive relationship between $\boldsymbol{\sigma}$ and $\boldsymbol{\epsilon}$.

3.2. Equilibrium in integral form

Let us introduce two kinematic admissibility spaces at the current configuration:

$$\mathcal{U} = \{\mathbf{u}|\mathbf{u} \text{ is sufficiently regular on } \boldsymbol{\Omega}, \mathbf{u} = \bar{\mathbf{u}} \text{ on } \partial\boldsymbol{\Omega_u}\} \qquad (37)$$

$$\mathcal{U}^0 = \{\mathbf{z}|\mathbf{z} \text{ is sufficiently regular on } \boldsymbol{\Omega}, \mathbf{z} = \mathbf{0} \text{ on } \partial\boldsymbol{\Omega_u}\}. \qquad (38)$$

16

Following Bathe (1996) and De Borst et al. (2012), the Principle of Virtual Work can be used to obtain the variational form of (33-36) as:

$$\int_{\Omega} \boldsymbol{\sigma} : \frac{1}{2}(\nabla \delta \mathbf{u} + \nabla \delta \mathbf{u}^{\top}) \, \mathrm{d}\boldsymbol{\Omega} = \int_{\Omega} \mathbf{b} \cdot \delta \mathbf{u} \, \mathrm{d}\boldsymbol{\Omega} + \int_{\partial \boldsymbol{\Omega}} \mathbf{p} \cdot \delta \mathbf{u} \, \mathrm{d}\partial \boldsymbol{\Omega} \qquad \forall \delta \mathbf{u} \in \mathcal{U}^{\mathbf{0}}$$

(39)

The superscript "$\top$" denote transpose. Since large deformations may occur, the equation (39) cannot be applied directly because the current valve configuration is unknown. On the other hand, the initial configuration (Ω_0) is known, and therefore the stress and strain quantities can be rewritten so that they always refer to it. Let τ represent the Second Piola–Kirchhoff stress tensor and $\mathbf{E}$ the Green–Lagrange strain tensor. Then, the following relations may be defined:

$$\mathbf{F} = \frac{\partial \mathbf{x}}{\partial \mathbf{X}}$$

(40)

$$\delta \mathbf{E} = \frac{1}{2} \mathbf{F}^{\top} (\nabla \delta \mathbf{u} + \nabla \delta \mathbf{u}^{\top}) \mathbf{F}$$

(41)

$$\tau = (\det \mathbf{F}) \mathbf{F}^{-\mathbf{1}} \boldsymbol{\sigma} \mathbf{F}^{-\top}$$

(42)

where $\mathbf{F}^{-\mathbf{1}}$ is the inverse of $\mathbf{F}$ and $\mathbf{F}^{-\top}$ indicate the transpose of $\mathbf{F}^{-\mathbf{1}}$.

Then, the equilibrium can then be rewritten as:

$$\int_{\Omega_0} \tau : \delta \mathbf{E} \, \mathrm{d}\Omega = \int_{\Omega_0} \mathbf{b} \cdot \delta \mathbf{u} \, \mathrm{d}\boldsymbol{\Omega} + \int_{\partial \boldsymbol{\Omega_0}} \mathbf{p_0} \cdot \delta \mathbf{u} \, \mathrm{d}\partial \boldsymbol{\Omega} \qquad \forall \delta \mathbf{u} \in \mathcal{U}^{\mathbf{0}} \qquad (43)$$

where $\mathbf{p_0}$ is the nominal traction (force per unit area at the initial configuration). This statement is known as the *Total Lagragian* formulation.

The second Piola-Kirchhoff stress tensor is symmetric and is related to the Green-Lagrange strain tensor according to the St. Venant constitutive law:

$$\tau = \lambda \mathrm{tr}(\mathbf{E})I + 2\mu \mathbf{E}$$

(44)

where λ and μ are the Lamé constants (material properties), and I is the second order unit tensor.

This formulation takes into account not only the change of configuration due to large displacements but also the existence of the initial stress state.

3.3. Contact modelling

Considering contact forces in the present model poses additional challenges because the interfaces move a great deal relative to each other. This causes not only the region in contact to vary, but also the alternation between zones that were in contact but now are no longer. In general, one can monitor the contact using the discrized domain through three different approaches:

(i) Node-to-node contact elements. The elements stipulate pairs of mesh nodes that will have their relative distances monitored during the analysis. This approach is suitable for point-to-point contact applications with small relative sliding.

(ii) Node-to-surface contact elements. In this case, the shortest distance between the nodes and the contacting surfaces are monitored. This approach is suitable for cases of large relative sliding, large deformations and non-conforming meshes. However, there can be convergence issues if the surface in contact presents discontinuities.

(iii) Surface-to-surface contact elements. The elements track the shortest distance between the surfaces in potential contact. This approach is suitable for problems involving large deformations and large relative sliding, and can also deal with interface discontinuities due to discretisation. This is the approach chosen for the present study.

The non-penetration condition is imposed along the contacting interface (Γ^c) using the Kuhn–Tucker relations in the normal direction:

$$g_n \geq 0, \quad q_n \leq 0, \quad g_n q_n = 0, \quad \mathbf{x} \in \mathbf{\Gamma^c} \tag{45}$$

with $q_n = \mathbf{q} \cdot \mathbf{n}$ denoting the normal contact force and $g_n = [\![\mathbf{u}]\!] \cdot \mathbf{n}$ the normal displacement jump.

For tangential direction, Coulomb's friction law is assumed:

$$c_f = |q_t| - \mu_f |q_n| \begin{cases} = 0, & \text{slip} \\ < 0, & \text{stick} \end{cases} \tag{46}$$

where μ_f is the Coulomb's friction coefficient, $q_t = \mathbf{q} \cdot \mathbf{m}$ is the tangential component of the contact force and $\mathbf{m}$ is the unit tangent vector along the

18

sliding direction. Similarly, letting $g_t = [\![\mathbf{u}]\!] \cdot \mathbf{m}$, the Kuhn-Tucker relation is established:

$$g_t \geq 0, \quad c_f \leq 0, \quad g_t c_f = 0, \quad \mathbf{x} \in \mathbf{\Gamma^c}. \tag{47}$$

The contact virtual work can be expressed as:

$$\delta w_c = \int_{\Gamma^c} q_n \mathbf{n} \cdot \delta \mathbf{u} + q_t \mathbf{m} \cdot \delta \mathbf{u} \ \mathrm{d}\mathbf{\Gamma^c} \qquad \forall \delta \mathbf{u} \in \mathcal{U}^0. \tag{48}$$

3.4. Linearized Problem and Finite Element discretization

Once the integral formulation is established, a finite element discretization Ω^h of Ω_0 is defined. This discretization is such that inside each finite element $\Omega_{0e} \in \Omega^h$ the unknown field $\mathbf{u}$ can be approximated from its nodal values ($\mathbb{U}$) through polynomial shape functions ($[\mathbb{H}]$ in matrix form), $\mathbf{u} = [\mathbb{H}]\mathbb{U}$. Following Sung and Kwak (2002), linearising equation (43) and (48), one obtains the expression for calculating the nodal displacement increments ($\Delta\mathbb{U}$), which reads as follows:

$$([\mathbb{K}_L] + [\mathbb{K}_{NL}])\Delta\mathbb{U} = \mathbb{F}_{ext}^{t+\Delta t} - \mathbb{F}_{int}^{t} + \mathbb{F}_{c}^{t+\Delta t} \tag{49}$$

where,

$$\mathbb{F}_{ext}^{t+\Delta t} = \mathbf{A} \int_{\Omega_{0e}} [\mathbb{H}]^{\top} \mathbf{b} \ \mathrm{d}\Omega + \mathbf{A} \int_{\partial\mathbf{\Omega_{0e}}} [\mathbb{H}]^{\top} \mathbf{p_0} \ \mathrm{d}\partial\Omega \tag{50}$$

$$\mathbb{F}_{int}^{t} = \mathbf{A} \int_{\Omega_{0e}} [\mathbb{B}_L]^{\top} \tau^{t} \ \mathrm{d}\Omega \tag{51}$$

$$\mathbb{F}_{c}^{t+\Delta t} = \mathbf{A} \int_{\Gamma_{0e}^{c}} [\mathbb{H}]^{\top} (q_n \mathbf{n} + q_t \mathbf{m}) \ \mathrm{d}\mathbf{\Gamma^c} \tag{52}$$

$$[\mathbb{K}_L] = \mathbf{A} \int_{\Omega_{0e}} [\mathbb{B}_L]^{\top} [\mathbb{D}][\mathbb{B}_L] \ \mathrm{d}\Omega \tag{53}$$

$$[\mathbb{K}_{NL}] = \mathbf{A} \int_{\Omega_{0e}} [\mathbb{B}_{NL}]^{\top} [\mathbb{T}][\mathbb{B}_{NL}] \ \mathrm{d}\Omega \tag{54}$$

In these expressions, $\mathbf{A}$ denotes the standard assembling operator over all elements of Ω^h. Γ_0^c represents the potential contact surfaces at the reference configuration. $[\mathbb{B}_L]$ is a matrix that depends on the shape function derivatives and that converts the nodal displacements to the linear part of strains.

19

Similarly, $[\mathbb{B}_{NL}]$ depends on the shape function derivatives and relates the nodal displacements to the non-linear portion of the strains. The matrix $[\mathbb{D}]$ contains the instantaneous stiffness of the material model and $[\mathbb{T}]$ collects the second Piola-Kirchhoff components.

3.5. Solution Technique

Equation (49) is used to build an iterative incremental scheme. Starting from a known solution ($\mathbb{U}^n$), an increment $\Delta\mathbb{U}$ is sought so that the residual forces ($\mathbb{L}$) are zero, that is:

$$\mathbb{L} = \mathbb{F}_{ext}^{t+\Delta t} - \mathbb{F}_{int}^{t} + \mathbb{F}_{c}^{t+\Delta t} = 0 \tag{55}$$

The residual is rarely zero on the first try, in particular when different sources of nonlinearity are included. For this reason the unbalanced forces from the previous iteration (k) are used to correct the nodal displacements, so that:

$$([\mathbb{K}_L] + [\mathbb{K}_{NL}])^k \Delta\mathbb{U}^{k+1} = \mathbb{L}^k \tag{56}$$

The iterations continue until the residue in the forces is sufficiently small. In this situation the converged nodal displacement $\mathbb{U}^{n+1}$ is obtained by adding all the corrections:

$$\mathbb{U}^{n+1} = \mathbb{U}^n + \Delta\mathbb{U} \tag{57}$$

$$\Delta\mathbb{U} = \sum_{k=1}^{NT} \Delta\mathbb{U}^k \tag{58}$$

where NT is the total number of iterations required for convergence. This process belongs to the class of incremental iterative Newton-based methods. In the present study, it was implemented using Ansys Mechanical® 2021.R2 solver.

3.6. Problem setting

From the equations developed in Section 2, three sets of parameters were chosen, resulting in three distinct geometries. Figure 9 illustrates the finite element mesh used for each of the geometries. Both the bottom ring of the valves and the three vertical edges (leaflets intersection) have constraint
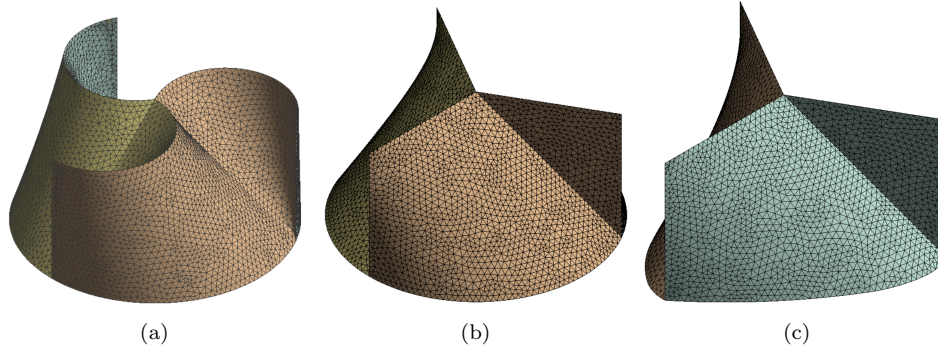
Figure 9: Finite Element Meshes: (a) Geometry 1 (5841 nodes, 11292 elements), (b) Geometry 2 (4839 nodes, 9372 elements), (c) Geometry 3 (4399 nodes, 8501 elements).

Table 1: Input parameters for the mechanical models

Parameter	Description	Value
ν_r	Poisson's ratio	0.49
E	Young modulus	$6, 5$ MPa
h_l	Leaflet thickness	$500 \ \mu$m
ν, n, m, κ	Geometry 1 parameters	$1, 1, 1, 0$
ν, n, m, κ	Geometry 2 parameters	$1, 0, 1, 0$
ν, n, m, κ	Geometry 3 parameters	$5, 0, 1, 0$

displacements and free rotations. The input parameters can be found in Table 1.

The numerical test consists in reproducing an operating cycle for each of the three valves. This cycle has four movements: (1) starting from the relaxed position to the maximum opening (2) returning from the maximum opening point to the relaxed position (3) starting from the relaxed position to the maximum closing point, and (4) returning from the maximum closing point to the relaxed position. The movement will be caused by an equally distributed pressure on the surface of the leaflets; its values are illustrated in Figure 10.

Figures 11 to 13 illustrate the designs obtained when the three-dimensional curves of the leaflets are unfolded onto a plane. One can clearly see the effect that parameters ν, n, m, κ have on the final leafltet geometry. Although they all have the same height along the axial axis of the valve, the resulting surface areas are substantially different.

21
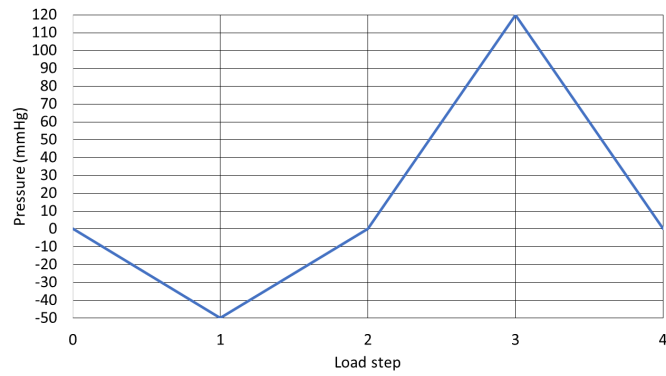
Figure 10: Pressure values applied at each loading step.

4. Results

The results obtained from the non-linear mechanical models are presented in Figures 14 up to Figure 31. These results are divided into two groups that characterize the opening and closing mechanisms of the three valves considered.
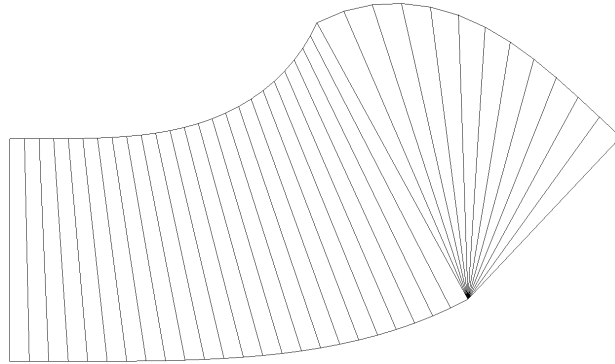
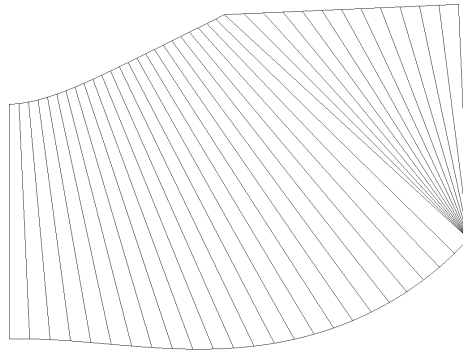Figure 11: Geometry 1 - Unfolding of leaflet shape onto the plane.

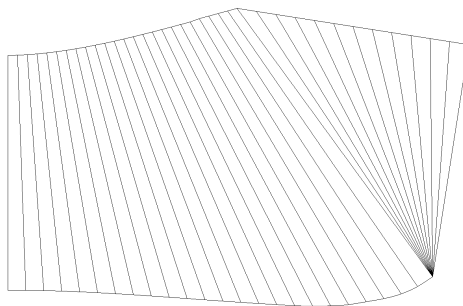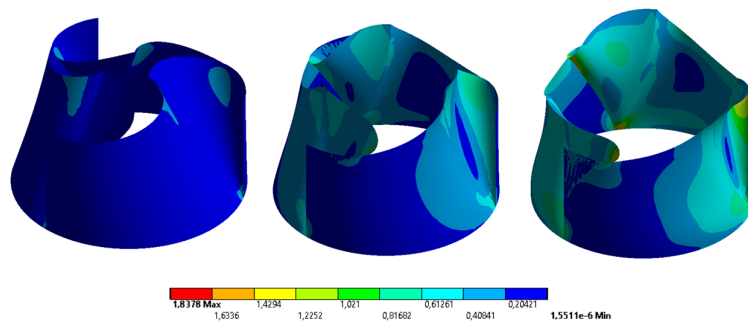Figure 12: Geometry 2 - Unfolding of leaflet shape onto the plane.

Figure 13: Geometry 3 - Unfolding of leaflet shape onto the plane.

Figure 14: Geometry 1 opening - Von Mises stress distribution corresponding to 20%, 50% and 100% of total load (from left to right). Units in MPa.
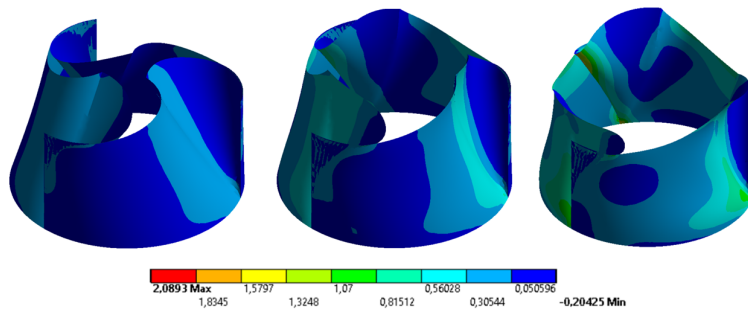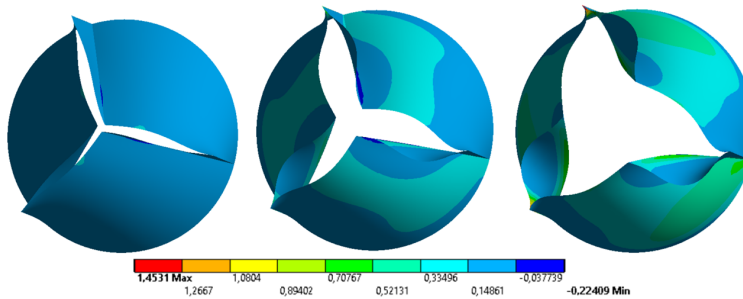

Figure 15: Geometry 1 opening - Maximum principal stress corresponding to 20%, 50% and 100% of total load (from left to right). Units in MPa.
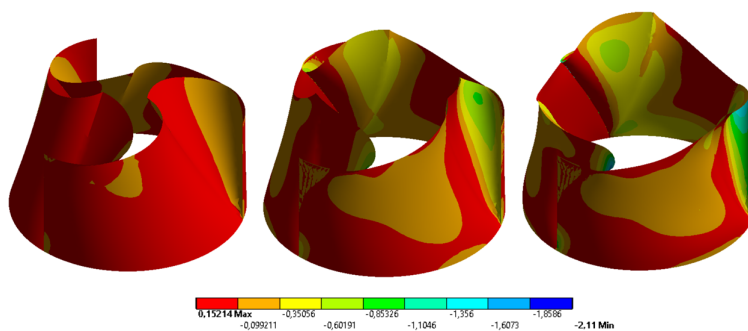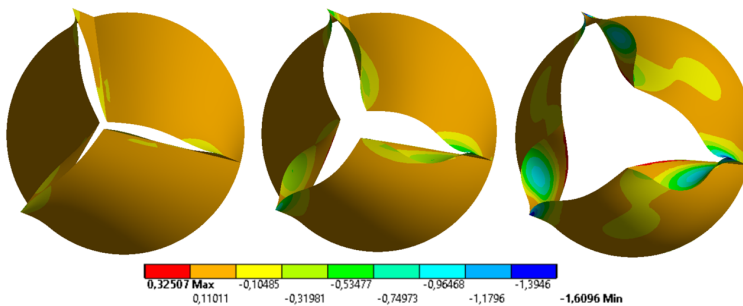

Figure 16: Geometry 1 opening - Minimum principal stress corresponding to 20%, 50% and 100% of total load (from left to right). Units in MPa.
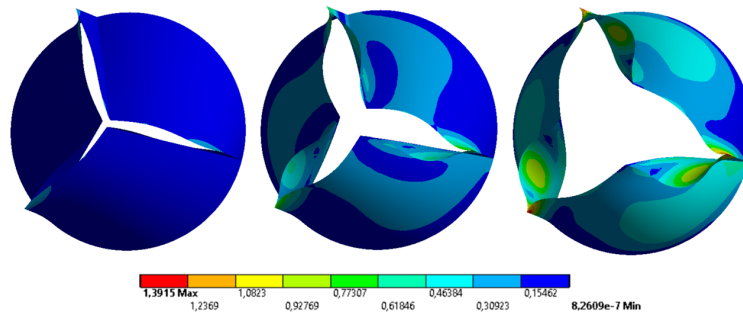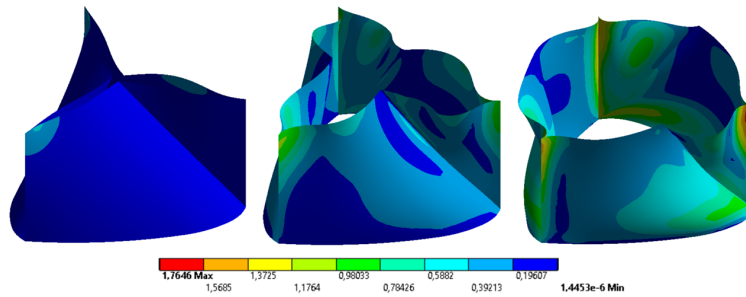
Figure 17: Geometry 2 opening - Von Mises stress distribution corresponding to 20%, 50% and 100% of total load (from left to right). Units in MPa.
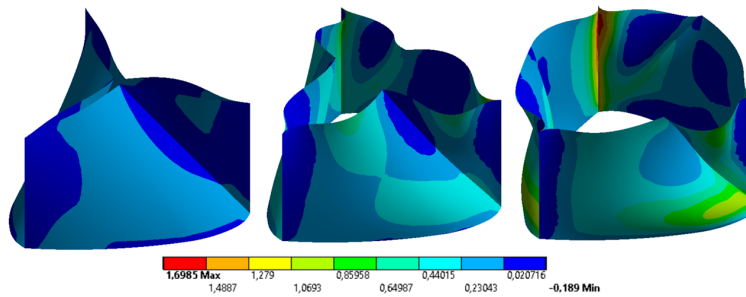

Figure 18: Geometry 2 opening - Maximum principal stress corresponding to 20%, 50% and 100% of total load (from left to right). Units in MPa.

Figure 19: Geometry 2 opening - Minimum principal stress corresponding to 20%, 50% and 100% of total load (from left to right). Units in MPa.

Figure 20: Geometry 3 opening - Von Mises stress distribution corresponding to 20%, 50% and 100% of total load (from left to right). Units in MPa.

Figure 21: Geometry 3 opening - Maximum principal stress corresponding to 20%, 50% and 100% of total load (from left to right). Units in MPa..
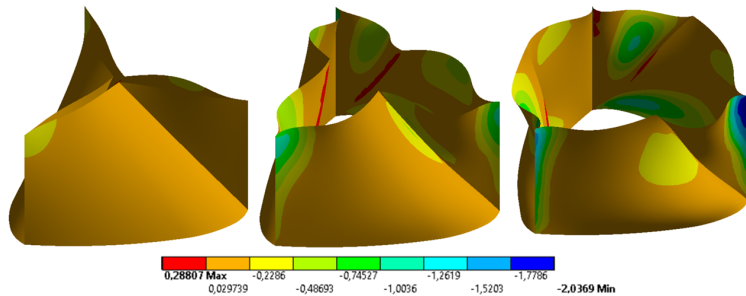

Figure 22: Geometry 3 opening - Minimum principal stress corresponding to 20%, 50% and 100% of total load (from left to right). Units in MPa..
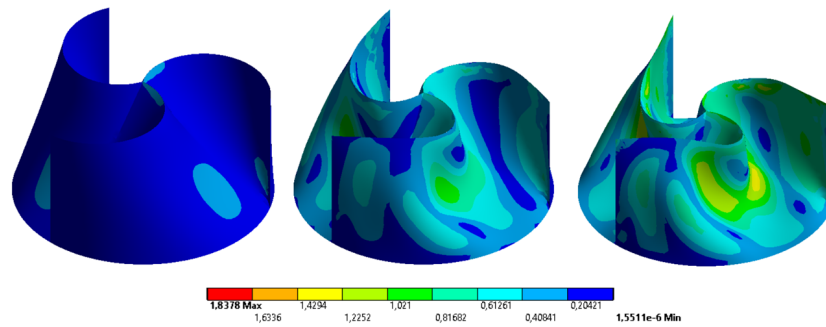
Figure 23: Geometry 1 closing - Von Mises stress distribution corresponding to 20%, 50% and 100% of total load (from left to right). Units in MPa.
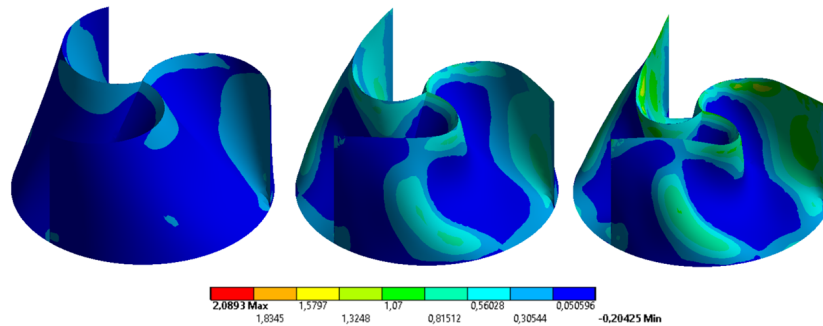

Figure 24: Geometry 1 closing - Maximum principal stress corresponding to 20%, 50% and 100% of total load (from left to right). Units in MPa.

Figure 25: Geometry 1 closing - Minimum principal stress corresponding to 20%, 50% and 100% of total load (from left to right). Units in MPa.

27

Figure 26: Geometry 2 closing - Von Mises stress distribution corresponding to 20%, 50% and 100% of total load (from left to right). Units in MPa. (units MPa)
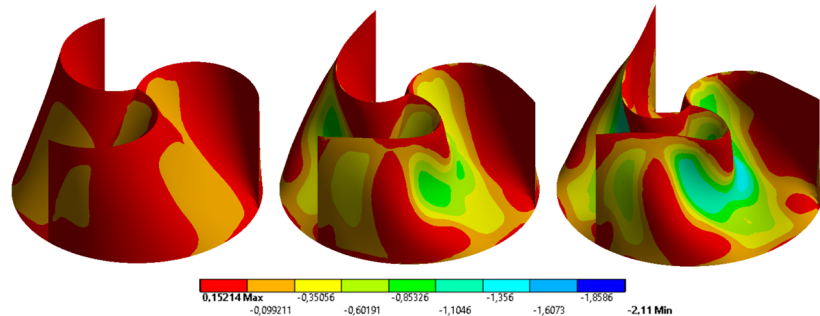

Figure 27: Geometry 2 closing - Maximum principal stress corresponding to 20%, 50% and 100% of total load (from left to right). Units in MPa.

Figure 28: Geometry 2 closing - Minimum principal stress corresponding to 20% , 50% and 100% of total load (from left to right). Units in MPa.
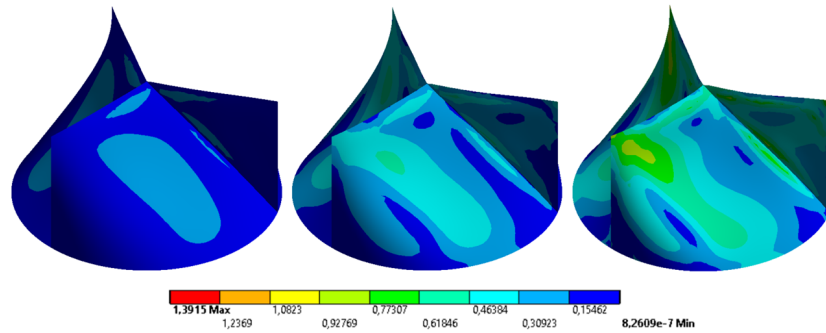
Figure 29: Geometry 3 closing - Von Mises stress distribution corresponding to 20%, 50% and 100% of total load (from left to right). Units in MPa.
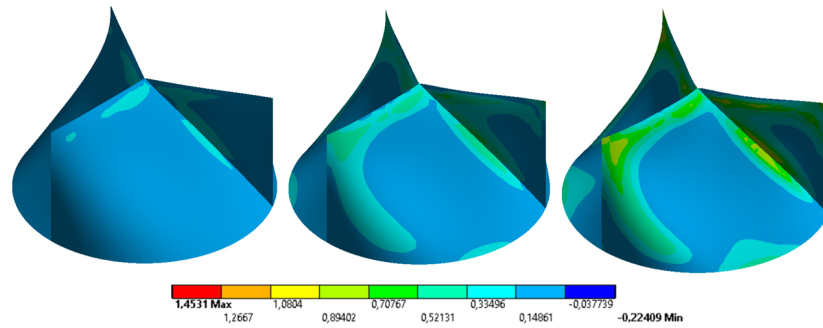

Figure 30: Geometry 3 closing - Maximum principal stress corresponding to 20%, 50% and 100% of total load (from left to right). Units in MPa.
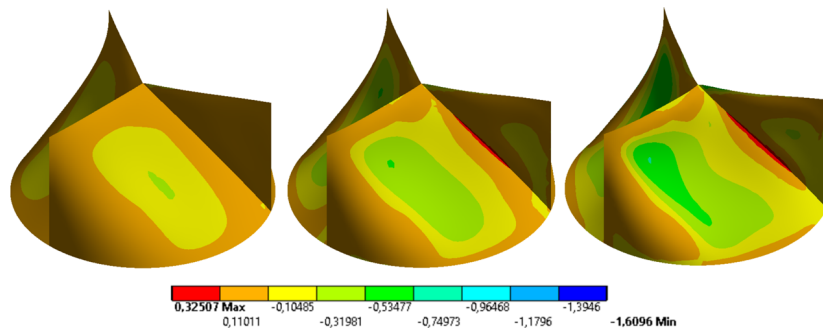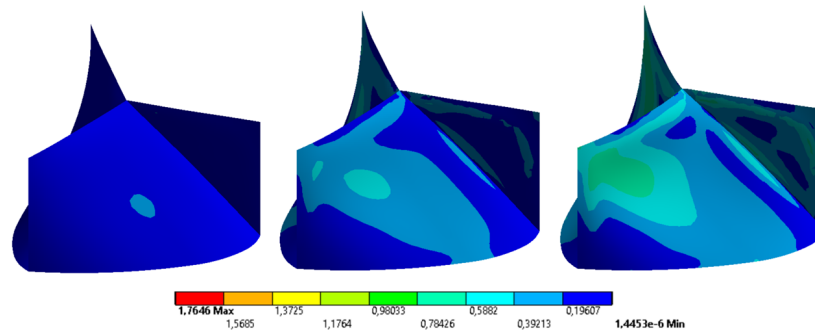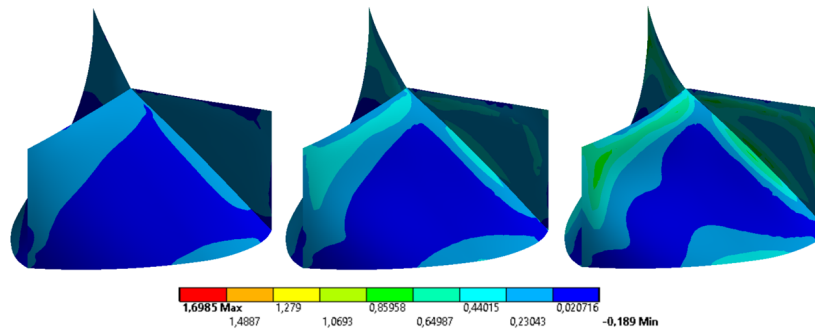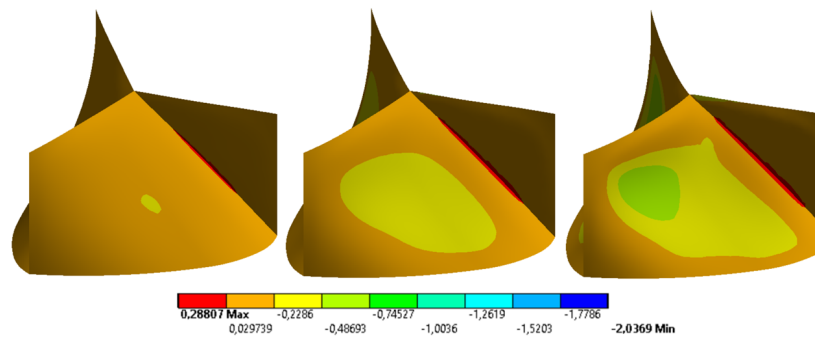

Figure 31: Geometry 3 closing - Minimum principal stress corresponding to 20% and 100% of total load (from left to right). Units in MPa.

5. Discussion

As illustrated in Figures 14 to Figure 31, mechanical analyses indicate that the overall operation of the valve can be understood according to two independent mechanisms: opening and closing. Both movements are induced by means of a static pressure field evenly distributed among all leaflets. In order to ensure equilibrium stability, internal stress fields are generated for each of the loading levels. These fields have different patterns depending on the considered mechanism and also on the geometry. In the discussion that follows, three stress fields will receive attention: Von Mises, Maximum Principal and Minimum Principal.

Geometry 1 - opening. Figures 14 through 16 display the stress fields for three different load factors during the opening phase. It can be seen that the global equilibrium is maintained through the simultaneous action of membrane and bending forces. Although the thickness of the leaflet is very small (around 26 times smaller compared to the characteristic height of the real valve (cf. Fig.1)), no predominance of membrane responses is observed. The pressure applied is sufficient to open the valve fully. Opening is accompanied by local changes in curvature that can be captured because equilibrium is always evaluated taking into account geometric non-linearities. Although stresses tend to be concentrated in the region of change of curvature and at the corners, the opening in general takes place in a stable manner, even with non-linear contacts activated between pairs of leaflets.

Geometry 2 - opening. The stress fields can be seen in Figures 17 to 19. Although Geometry 2 shows similarities with Geometry 1, the overall mechanical behaviour is slightly different. The straight position at the top edges means that a greater mechanical energy needs to be supplied to the leaflets to move them from their different opening position. The direct result is that the structure shows itself to be less flexible which means that it opens less for the same level of applied pressure. As in Geometry 1, but in a more pronounced way, stress concentrations occur at the zone of abrupt change of curvature. The stresses tend to spread producing localised bending zones that favours the opening of leaflets. The contact forces that stabilise the motion depend directly on the opening positions of the leaflets. High mesh distortions have potentially a negatively impact on convergence, but here this effect is not observed.

30

Geometry 3 - opening. The stress fields illustrated in Figures 20 to 22 show some difference compared to the previous two. Note that the valve base has leaflets no longer through arcs of circles, but rather through arcs of ellipses. Zones of stress concentration still occur at corners and where leaflets change curvature. However, stresses tend to spread more evenly throughout the leaflets. The result is that the valve structure can accumulate more elastic energy for the same level of external loading. One can notice that total opening is close to Geometry 1, but with smaller surface area. Local bending is also present in this geometry but it does not have a negative impact on the stability or contact forces.

Geometry 1 - closing. Figures 23 to 25 illustrate the stress fields generated in response to the acting pressure. These fields show that valve closing depends on two actions occurring simultaneously: large deformations increasing elastic energy and contact forces (preventing penetration between leaflets). On closing, the leaflets produce two movements: vertical downward displacement and rotation about the axial axis of the valve. This rotation occurs because the leaflets push each other in a spiral direction (with a twisting motion) performing exactly the function for which they were designed. As with opening, elastic buckling is also observed within the compression zones, which can cause convergence problems due to high mesh distortions. In these cases, dynamic meshing can be helpful. However, for the pressure levels applied, this procedure was not necessary. The movement of the leaflets responds to a combination of both membranous and fexural internal forces. The formation of a convex shape ("bag shape") in the region near the supports is also noted. This geometrical configuration closely resembles the shapes found in artificial designs inspired by the human aortic valves (e.g. Ghosh et al. (2018)).

Geometry 2 - closing. In the case of the second geometric shape, the corresponding stress fields are illustrated in Figures 26 to 28. The straight shape of the upper edge of the leaflets provides a greater stiffness to closing when compared to Geometry 1. This effect is similar to that observed in the opening phase. Although the leaflets tend to form a convex shape in the region near the vertical supports, the amplitude is less pronounced than that in Geometry 1. In this way, leaflets tend to remain vertical when moved downwards, which leads to the elimination of twisting movements. Elastic buckling is also less prevalent in compressive stress regions, which illustrates the lower flexibility conferred by the global shape.

Geometry 3 - closing. For the third geometric shape, the corresponding stresses are illustrated in Figures 29 to 31. For closing motions, this geometry is more rigid when compared to Geometry 1. However, the exchange of the circular arcs at the base for elliptical ones gives slightly more flexibility when compared to Geometry 2. As in the previous case, the compression zones also do not manifest elastic instabilities, and the overall shape is preserved throughout the movement. Convex compression zones tend to form, but not in pronounced amplitude as in Geometry 1. The stresses tended to concentrate at the corners and at the regions of drastic curvature change. However, there was no need for remeshing to improve convergence.

Boundary Conditions. It is worth mentioning that, in realistic opening conditions, the valve is not under the action of static pressures, but dynamic ones which vary according to the position of each leaflet. However, when closing, the assumption of static pressure is reasonable as the remaining flow movements do not significantly alter the pressure exerted on the valve surface. Despite the simple assumptions adopted for the boundary conditions, the mechanical response observed in the present numerical experiments acquire greater relevance in the closing phase.

As can be seen from this discussion, the mechanical behaviour of artificial valves based on the Wheatley design are directly impacted by the geometries of the leaflets. For this reason, having analytical representations that describe, even approximately, the initial configuration is of immense help for decision making in the design and optimisation phase. What has been explored here demonstrates the influence of key modelling assumptions, not only geometric but also in regards to possible stress model comparisons. This will be crucial for the development of the Wheatley valve when future pulse duplicator testing and fatigue testing of the geometric variants and models will take place as the valve's functionality is optimised both theoretically and experimentally. In addition to direct applications to the Wheatley valve design, the equations proposed in Section 2 have the potential to be extended to other devices or structural systems that have similar characteristics, in particular for shell-based shapes where analytical descriptions are rarely available.

6. Conclusion

The present study addressed a generalisation of the mathematical representation of the Wheatley aortic valve. In a previous work, McKee et al. (2021) considered the cross section of each leaflet as being obtained from the union of two arcs of circles. This time, these arcs were replaced by elliptical arcs controlled by a small number of parameters. These parameters control not only the degree of ellipticity employed, but also the shape that the leaflets acquire along the height of the valve. This makes the work presented by McKee et al. (2021) a particular case of the present analytical formulation.

Descriptions such as these are an important prerequisite when studying different geometric alternatives that may be employed at the design stage. To illustrate its application, we chose three distinct sets of parameters, which in turn gave rise to three distinct Wheatley valve geometries. Each geometry was used to build a non-linear computational mechanical model that can be used to simulate the opening and closing motions.

The analysis of the results allows us to emphasise some aspects:

(i) The combination of analytical geometric description (Section 2) and computational mechanical modelling (Section 3) produces an efficient methodology for the investigation of innovative designs. It is possible to directly infer the influence that a given geometric parameter has on the distribution of the final equilibrium stresses.

(ii) This methodology can be directly applied to other studies involving different valves or prosthetic organs, provided that an analytical geometric description representing the structure under attention is available.

(iii) The four parameters controlling the overall shape of the leaflets, and ultimately the valve geometry itself, can be used for optimization purposes based on mechanical performance.

(iv) The minimum properties that a mechanical model needs in order to properly capture the opening and closing movements of the WHV under the action of normal static pressures are: evaluate the balance of forces in the displaced position, non-linear contacts between leaflets and linear constitutive response. Depending on the actual material used, non-linear constitutive laws may be necessary to obtain improved results.

The present study can be extended to incorporate additional equations that ensure the continuity of the normal vector along the line where two leaflets intersect. Moreover, the proposed equations can be used in isogeometric modelling (Hughes et al. (2005)), as they do not need to undergo Lagrangian polynomial discretization.

Acknowledgment

References

M. Riedel, A. Streit, F. Wolf, T. Lippert, D. Kranzlmüller, Classification of different approaches for e-science applications in next generation computing infrastructures, in: 2008 IEEE Fourth International Conference on eScience, IEEE, 2008, pp. 198–205.

A. D. Kaiser, R. Shad, W. Hiesinger, A. L. Marsden, A design-based model of the aortic valve for fluid-structure interaction, Biomechanics and Modeling in Mechanobiology 20 (2021) 2413–2435.

M. B. Jatene, R. Monteiro, M. H. Guimarães, S. C. Veronezi, M. K. Koike, F. B. Jatene, A. D. Jatene, Aortic valve assessment. anatomical study of 100 healthy human hearts, Arquivos brasileiros de cardiologia 73 (1999) 81–86.

J. Ghanbari, A. Dehparvar, A. Zakeri, Design and analysis of prosthetic heart valves and assessing the effects of leaflet design on the mechanical attributes of the valves, Frontiers in Mechanical Engineering 8 (2022) 764034.

M. P. Bendsøe, Optimal shape design as a material distribution problem, Structural optimization 1 (1989) 193–202.

A. H. Khalighi, B. V. Rego, A. Drach, R. C. Gorman, J. H. Gorman, M. S. Sacks, Development of a functionally equivalent model of the mitral valve chordae tendineae through topology optimization, Annals of biomedical engineering 47 (2019) 60–74.

N. Jenkins, K. Maute, An immersed boundary approach for shape and topology optimization of stationary fluid-structure interaction problems, Structural and Multidisciplinary Optimization 54 (2016) 1191–1208.

A. Balu, S. Nallagonda, F. Xu, A. Krishnamurthy, M.-C. Hsu, S. Sarkar, A deep learning framework for design and analysis of surgical bioprosthetic heart valves, Scientific reports 9 (2019) 1–12.

O. A. Jarral, M. K. Tan, M. Y. Salmasi, S. Pirola, J. R. Pepper, D. P. O'Regan, X. Y. Xu, T. Athanasiou, Phase-contrast magnetic resonance imaging and computational fluid dynamics assessment of thoracic aorta blood flow: a literature review, European Journal of Cardio-Thoracic Surgery 57 (2020) 438–446.

M. Chaudhry, L. Raco, E. Muriithi, G. Bernacca, M. Tolland, D. Wheatley, Porcine versus pericardial bioprostheses: eleven-year follow up of a prospective randomized trial., The Journal of Heart Valve Disease 9 (2000) 429–37.

D. Wheatley, L. Raco, G. Bernacca, I. Sim, P. Belcher, J. Boyd, Polyurethane: material for the next generation of heart valve prostheses?, European journal of cardio-thoracic surgery 17 (2000) 440–448.

D. Wheatley, Heart valve, US Patent 9259313 (2014).

D. Wheatley, Heart valve, UK Patent EP2982340 (2016a).

D. Wheatley, Heart valve, European Patent EP2979666 (2016b).

C. S. Peskin, Flow patterns around heart valves: a numerical method, Journal of computational physics 10 (1972) 252–271.

X. Wang, L. T. Zhang, Modified immersed finite element method for fully-coupled fluid–structure interactions, Computer methods in applied mechanics and engineering 267 (2013) 150–169.

W. Sun, C. Martin, T. Pham, Computational modeling of cardiac valve function and intervention, Annual review of biomedical engineering 16 (2014) 53–76.

J. H. Spühler, J. Jansson, N. Jansson, J. Hoffman, 3d fluid-structure interaction simulation of aortic valves using a unified continuum ale fem model, Frontiers in physiology 9 (2018) 363.

S. S. Abbas, M. S. Nasif, R. Al-Waked, State-of-the-art numerical fluid–structure interaction methods for aortic and mitral heart valves simulations: A review, Simulation 98 (2022) 3–34.

S. McKee, J. A. Cuminato, I. Stewart, D. Wheatley, A mathematical representation of the wheatley heart valve, Journal of Biomechanical Engineering 143 (2021).

K.-J. Bathe, Finite element procedures in engineering analysis, Prentice Hall, 1996.

R. De Borst, M. A. Crisfield, J. J. Remmers, C. V. Verhoosel, Nonlinear finite element analysis of solids and structures, John Wiley & Sons, 2012.

J. H. Sung, B. M. Kwak, Large displacement dynamic analysis with frictional contact by linear complementarity formulation, Computers & structures 80 (2002) 977–988.

R. P. Ghosh, G. Marom, O. M. Rotman, M. J. Slepian, S. Prabhakar, M. Horner, D. Bluestein, Comparative fluid–structure interaction analysis of polymeric transcatheter and surgical aortic valves' hemodynamics and structural mechanics, Journal of biomechanical engineering 140 (2018).

T. J. Hughes, J. A. Cottrell, Y. Bazilevs, Isogeometric analysis: Cad, finite elements, nurbs, exact geometry and mesh refinement, Computer methods in applied mechanics and engineering 194 (2005) 4135–4195.